PCCP

Accepted Manuscript

Volume 1 | Number 1 | Jan 2013 | Pages 1–100

PCCP

Physical Chemistry Chemical Physics
www.rsc.org/pccp

ROYAL SOCIETY OF CHEMISTRY

ROYAL SOCIETY OF CHEMISTRY

www.rsc.org/pccp

Physical Chemistry Chemical Physics

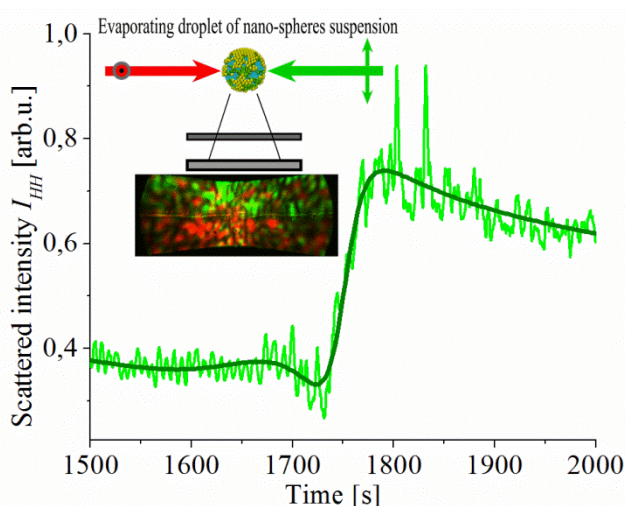Cite this: DOI: 10.1039/c0xx00000x

ARTICLE TYPE

www.rsc.org/xxxxxx

Surface Diagnostics of Evaporating Droplet of Nanospheres Suspension; Fano Interference and Surface Pressure

Maciej Kolwas, Krystyna Kolwas*, Gennadiy Derkachov and Daniel Jakubczyk

Evaporation of a single, levitating microdroplet of glycols containing SiO_2 nanospheres, both of similar refraction indexes, was studied by observing changes in the interference pattern and intensities of polarized and depolarized scattered laser light. Evolution of the droplet effective radius has been found on the base of Mie scattering theory supplemented by "electrical weighting" measurement of droplet mass
10 evolution. During formation of a layer of nanospheres on the droplet surface, the asymmetric Fano profile was observed which was found to be due to the destructive and constructive interference of overlapping processes: (i) the scattering on single nanospheres emerging on the droplet surface and (ii) the scattering on ensembles of closely spaced (comparing to the light wavelength) nanospheres of an evolving surface film. Thereby we report the first observation of the Fano interference in the time domain rather than in
15 spectral domain. The optical surface diagnostics was complemented with the thermodynamics-like analysis in terms of the effective droplet surface pressure isotherm and with numerical simulations illustrating evaporation driven changes in the distribution of nanospheres. The reported study can serve as the basis for a wide range of novel diagnostic methods of configuration changes in complex systems of nano- and microparticles evolving at the sub-wavelength scale.

Introduction

20 The concept of resonance is one of the most fundamental physical phenomena present in almost all branches of science. The specific type of resonances is described by the Fano spectral profile[1] which is widely studied in many branches of physics from
25 spectroscopy, quantum optics, to nanophotonics[2,3]. The Fano asymmetric profile arises as the result of a superposition of the constructive and the destructive interference, when a narrow or discrete-band resonance coincides with a broadband resonance. The Fano interference can be observed, among others, in
30 plasmonic nanostructures, photonic crystals, and metamaterials[4]. The interference leading to the asymmetric spectral profile appears in many scattering processes in photonics[5]. The Fano type resonances influence the efficiency of scattering of light on composite materials with a sophisticated effective index of
35 refraction: metamaterials, layered materials and photonic crystals. These materials are of high interest to optoelectronics and photonics applications[6-10].
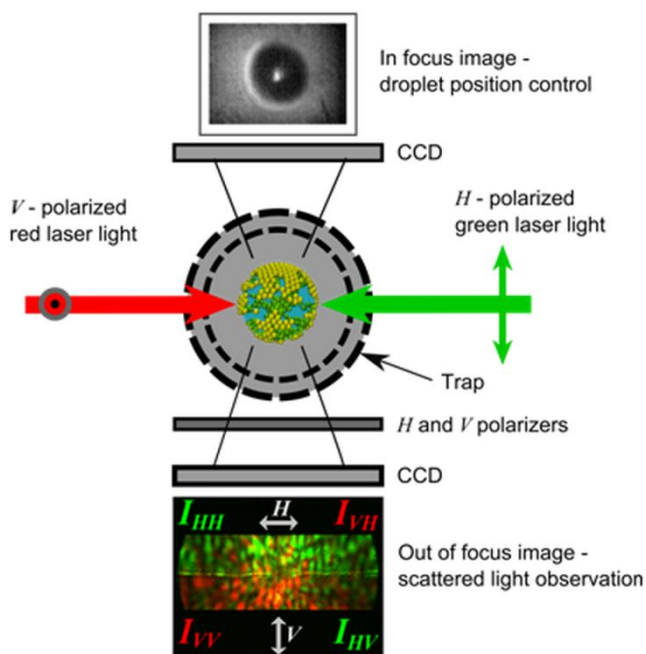
Figure 1 The scheme of experimental set-up. Top: droplet position stabilization system, middle: geometry of the trap, illumination and observation channels. Bottom: out of focus image acquisition of the dynamic interference pattern (the example pattern at the late stage of evaporation) after passing by upper: *H* (horizontally) and lower: *V* (vertically) aligned polarizers in the detection channel.

In this paper we report the first observation of the Fano profile in the time domain rather than in spectral domain. The observed Fano profile develops as the result of an interference of electromagnetic (EM) fields scattered by an evaporating droplet of monodisperse nanospheres (NSs) suspension. Since the indices of refraction of liquids and NSs were similar, the volume optical inhomogeneities could be neglected. On the contrary, during evaporation of a the liquid from a droplet, NSs were emerging on the droplet surface, which significantly influenced the intensity and the polarisation of the scattered laser light[11,12]. The Fano profile was observed during the evaporation stage, when single NSs on the droplet surface aggregate into a film. Our analysis suggests that the temporally overlapping processes which contribute to the observed Fano interference are: (i) the long lasting scattering of EM field on the droplet with single NSs emerging on the surface of a drying droplet, and (ii) the scattering on ensembles of NSs, in which the distance between NSs becomes comparable to the light wavelength[13]. The last process takes place at the short-lasting evolution stage, when the compressible layer of NSs at the droplet surface is formed. The interpretation of the temporal Fano profiles is supported by the surface thermodynamic-like analysis of the droplet effective surface pressure. We also illustrate the changes in NSs distribution driven by shrinking of the droplet, with numerical simulations.

Experimental set-up, geometry of observation, sample preparation and signal processing

Single evaporating droplets of suspensions we studied were levitated in the electrodynamic quadrupole trap[14-17], which was
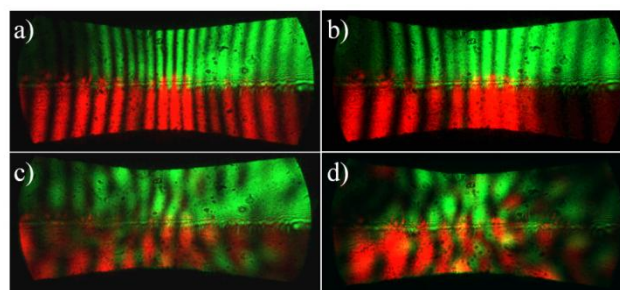

Figure 2 Examples of the interference patterns (the out-of-focus images) acquired during evaporation of a glycol droplet of SiO$_2$ spherical suspension. Upper half in figures a) – d): H polarization detection, lower half: V polarization detection.

built in our lab[13,18-20]. Droplets were injected into the trap with the droplet-on-demand injector (built in our lab as well), similar to the one described in [21,23]. The droplets were charged by charge separation in the external field of the trap, on emerging from the injector nozzle. Thus, the sign and, to some extent, the value of the charge was determined by the injection timing versus the phase of the trapping AC field. The vertical position of the trapped droplet was stabilised at the trap centre by balancing the weight of the droplet with the DC field. The trap was kept in a small ($\sim$10 cm^3) thermostatic chamber with dry nitrogen atmosphere at 25^{0}C and ambient atmospheric pressure. The droplet-on-demand injector was kept at chamber temperature. Our set-up allowed stable trapping of droplets of radius in the range from $\sim$35μm to $\sim$0.5μm. The average initial droplet radius was several micrometers. The geometry of experiment is shown in Figure 1.

We used simultaneously two coaxial, counter propagating laser light beams for droplet illumination: the red (658nm; 10mW) vertically (*V*) polarized and green (532nm; 5.5mW) horizontally (*H*) polarized in respect to the scattering plane (Figure 1). Two linear polarizes were used in the detection channel. *H*-polarizer (see upper half of the detection channel in Figure 1) enabled observation of the interference pattern of horizontally polarized light with intensities $I_{HH}(\phi,\Theta;t)$ (green light with the unchanged polarization) and $I_{VH}(\phi,\Theta;t)$, (red, cross-polarized light). *V*-polarizer (lower half of the detection channel in Figure 1) enabled detection of the interference pattern of vertically polarized light with the intensities $I_{VV}(\phi,\Theta;t)$ (red light with the unchanged polarization) and $I_{HV}(\phi,\Theta;t)$ (green, cross-polarized light). Temporal dependence of the scattered interference patterns was registered with CCD camera and recorded. Figure 2 contains some snapshots from an example movie at different stages of droplet evaporation. Upper half (*H*-polarization detection) of Figure 2 a) shows green fringes with the intensity $I_{HH}(\phi,\Theta;t)$ at the early stages of droplet evaporation. Fringes became less frequent with the decreasing droplet radius (see Figure 2 b)) and gradually undergo transformation into green speckles at the late stage of evaporation (see Figure 2 c)). Green speckles with the intensity $I_{HV}(\phi,\Theta;t)$ of the crossed polarization light appear also on the lower half of the detection channel (after *H*-polarization detection) (see Figure 2 c)) revealing depolarization of green scattered light at this stage of droplet evaporation. Similar applies to the interference pattern of red scattered light with the intensity
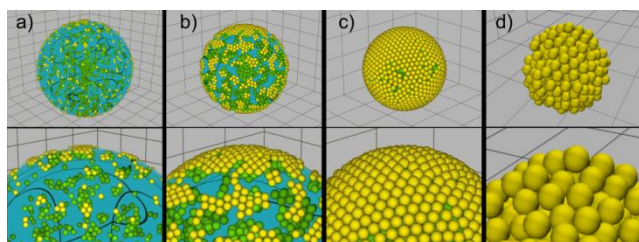
Figure 3 Evolution of the evaporating droplet of NSs suspension according to the numerical modelling. Snapshots illustrate evaporation-driven changes in NSs distribution. In the upper row: the droplet/crystallite size was normalized. Lower row: enlargements of the upper-row images.

$I_{VV}(\phi,\Theta;t)$ observed in the lower half of the detection channel (V-polarization detection). Red light also became depolarized with the progress of evaporation and leaks to the upper half of the detection channel (H-polarization) forming some speckles with

5 the intensity distribution $I_{HV}(\phi,\Theta;t)$. A color camera allowed us to separate the elastically scattered light spectrally and attribute their intensities to the appropriate incident beam polarization. Temporal evolution of the angular intensity distributions of the scattered light of intensities $I(\phi;\Theta;t)$ was recorded at an angle Θ

10 $= 90 \pm 16{:}24°$ (azimuth) and $\phi = 0 \pm 5{:}33°$ (elevation).

In order to find droplet radius evolution $a(t)$, we fitted Mie theory predictions[24] (with the look up table method) to the experimental regular interference patterns (fringes) $I_{VV}(\phi,\Theta;t)$ and $I_{HH}(\phi,\Theta;t)$ in the similar way as in our previous papers[11-13]. Additionally, the

15 droplet stabilisation voltage was used to measure the droplet mass evolution ("electrical weighting" method)[19]. As long as the droplet charge is constant, the DC voltage required to balance the droplet weight and keep the droplet in the centre of the trap is proportional to the droplet mass. Since our droplets are rather

20 weakly charged, we very rarely encounter the droplet charge loss (Coulomb explosion). Thus, due to operation of vertical stabilisation loop (see above), we obtain a signal proportional to the droplet mass. Since the number of NSs in the droplet/aggregate is constant, the final aggregate mass is equal to

25 the total mass of NSs. Subtracting it from the mass of the droplet yields the mass of liquid. Knowing the density of liquid and of NSs, we can find their respective volume changes. Since these volumes add (NSs are insoluble), the changes in the droplet/aggregate radius can be determined (it must be kept in

30 mind that at the stage of (nearly) dry aggregate the interstices between NSs are empty). However, the charge of the droplet is *a priori* unknown and the radius found from weighting must be calibrated with the optical method described above. This can be done at an early stage of evolution, when NSs concentration is

35 low and the optical method yields reliable results. The combination of these methods enabled very accurate determination of droplet radius for the entire droplet/aggregate evolution. In addition, the observed intensity distributions $I_{VV}(\phi,\Theta;t)$, $I_{HH}(\phi,\Theta;t)$, $I_{VH}(\phi,\Theta;t)$ and $I_{HV}(\phi,\Theta;t)$ were integrated

40 over angles of observation ϕ and Θ to obtain time dependent signals: $I_{VV}(t)$, $I_{HH}(t)$, $I_{VH}(t)$ and $I_{HV}(t)$ additionally characterising the progress of evaporation.

SiO_2 nano-spheres (C-SIO-0.45, Corpuscular) of 225-nm-radius were dispersed in two types of liquids: ethylene glycol (EG; 99.9
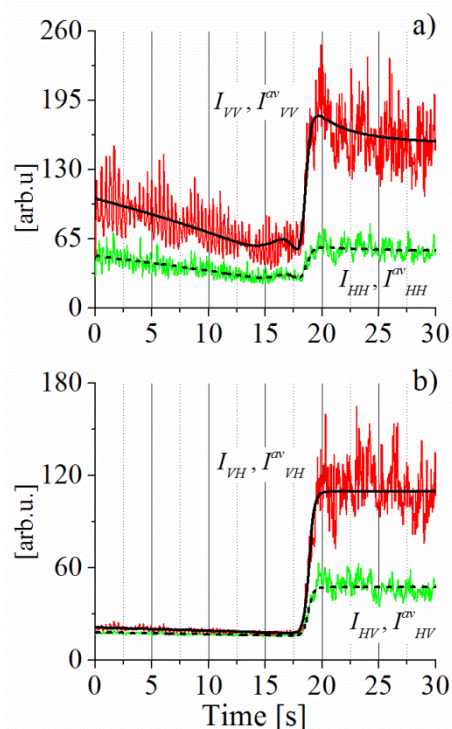

Figure 4 Temporal evolution of intensity of light scattered on a droplet of SiO_2 NSs suspension in ethylene glycol: a) $I_{VV}(t)$ (red line) and $I_{HH}(t)$ (green line) intensities of scattered light with polarization retained, b) $I_{VH}(t)$ (red line) and $I_{HV}(t)$ (green line) intensities of cross-polarized light. Black solid and dashed lines in a) and b) represent the corresponding average intensities.

45 GC area %, SPECTRANAL, Riedel-de Haen) and diethylene glycol (DEG; 99.99 GC area %, BioUltra, Fluka). The suspensions were prepared by first mixing EG or DEG with SDS and then with pre-concentrated suspension of SiO_2 nano-spheres in water. The approximate initial mass fractions were: SiO_2:EG

50 =1:200 with 0.1 SDS; SiO_2:DEG=1:250 (low concentration) or 1:130 (high concentration) with 0.1 SDS. The indices of refraction of the glycols used (ethylene glycol (EG): n =1.431 and diethylene glycol (DEG): n =1.447) was comparable to the refractive index of nanospheres (SiO_2: n = 1.463), so the volume

55 optical inhomogeneities during the evaporation process were small.

Evolution of the NSs distribution and light scattering

The scattering on a homogeneous droplet does not lead to light

60 depolarisation, so the cross-polarised I_{VH} and I_{HV} signals are absent in such case. Therefore, as long as the droplet is large and composed mainly of liquid (the volume fraction of NSs is small at early stages of droplet evolution), the intensities I_{VH} and I_{HV} of cross-polarised light are expected to be small and the droplet

65 surface to be spherical and smooth. Moreover, while indices of refraction of SiO_2 NSs and glycols are similar, the droplet at the early stage of evolution is expected to be optically homogeneous. The droplet surface loses its homogeneity and smoothness as the evaporating droplet shrinks and NSs from the evaporated volume
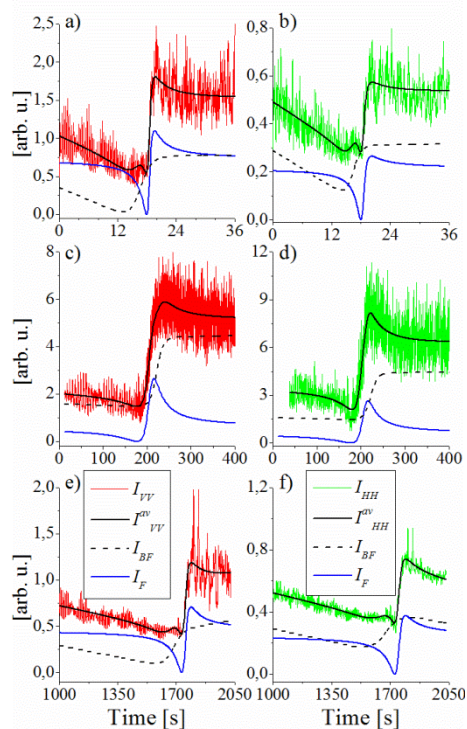
70 populate the surface.

Figure 5 Examples of the evolution of the scattered light intensity and the corresponding average intensities: a), b) EG with medium concentration of NSs (SiO$_2$:EG =1:200); c), d) DEG with low concentrations of NSs (SiO$_2$:DEG=1:250) and e), f) DEG with high concentrations of NSs (SiO$_2$:DEG=1:130). The Fano profile $I_F(t)$ and the sigmoid profile $I_{BF}(t)$ contributions to the corresponding $I^{av}(t)$ intensities are drown with solid blue and dashed black lines respectively.

We performed numerical simulations (similar to those described in[11]) which illustrate the consecutive stages of the evolution of the droplet of suspension. NSs were assumed to interact with forces resulting from the Lenard-Jones potential. Some characteristic stages are shown in Figure 3. The images a)–d) of Figure 3 illustrate the changes in distribution of NSs driven by the shrinking droplet which scatters light of the two orthogonally polarized laser beams (Figure 1). After injection of a droplet into the trap, the scattering of light on a (nearly) homogeneous droplet takes place. It is followed by scattering on a droplet with single, isolated NSs on the surface (Figure 3 a)). The distribution of NSs on the surface gradually evolves towards the transient islands (Figure 3 b)) and then the regularly packed NSs surface layer (Figure 3 c)). NSs form a kind of a quasi-regular diffraction grating. After the collapse of the NSs surface layer, light is scattered by a drying NSs' aggregate (Figure 3 e)). Contribution of scattering on single NSs becomes significant when NSs emerge on the droplet surface, (since refraction indices of glycols and SiO$_2$ NSs are very similar) and remains important until the end of observation of evaporation process. Rearrangement of NSs in the droplet volume is not reflected in the scattered intensities.

Generally, scattering on NSs is expected to consist of the contributions resulting from scattering on individual NSs (which in absence of other contributions would result in summation of intensities of light scattered on NSs) and of the coherent part[23], which gains importance for average distance between NSs comparable with the light wavelength[11,13]. In our experiment,

there is a stage of droplet evaporation, when scattering on individual NSs and on closely spaced NSs are present simultaneously. This enables interference of both scattering contributions. The Fano profile is expected to develop in time domain as the result of interference of EM fields originating from the short-lasting process of scattering on closely spaced NSs and the long-lasting process of scattering on individual NSs. Examples of observed temporal evolution of scattered light intensities are presented in Figures 4.

Evolution of the crossed-polarized scattered light intensities

The experimental cross-polarized (depolarized) intensities $I_{VH}(t)$ and $I_{HV}(t)$ (Figure. 4 b)) are small and constant during the first 18 seconds of droplet evolution. Starting from 18th second, $I_{VH}(t)$ and $I_{HV}(t)$ increase rapidly, and at 20th second they stabilise at a higher value. The increase in depolarization signifies that the scattering object loses its homogeneity. Since the droplet volume is nearly homogeneous, the inhomogeneity must be attributed solely to the roughness of the surface. Therefore, the increase in cross-polarized intensities means, that the formation of a surface layer of SiO$_2$ NSs takes place between 18th and 20th second of the droplet evolution.

The averages $I^{av}_{VH}(t)$ and $I^{av}_{HV}(t)$ over oscillations of cross-polarized intensities $I_{VH}(t)$ and $I_{HV}(t)$ can be well reproduced (see black solid and dashed lines Figure 4 b)) with a sigmoid (logistic) function of time $I_B(t)$:

$$I_B\,(t) = I_2 + (I_1 - I_2)/(1 + exp\left(\frac{t - t_0}{\Delta}\right)) \tag{1}$$

$I_B(t)$ describes change of scattered light intensity from the level I_1 to the level I_2. I_1 is a measure of the residual "background" signal up to ~17th second. In the ideal case of homogeneous, spherical droplet, I_1=0. I_2 is a measure of scattering by rough surface formed by NSs (t>20 seconds, Figure 4 b)). The parameter t_0 defines the centre of the transient region between 18th and 20th second, while Δ describes the duration of the transient region. The logistic function is extensively used in various branches of sciences, including biology, chemistry, sociology and economics, in studies of population growth with limited resources (see e.g.[26]). Successful application of the logistic function $I_B(t)$ (Eq.1) to modelling of depolarization of scattered light suggests that the (average) crossed-polarized intensities $I^{av}_{VH}(t)$ and $I^{av}_{HV}(t)$ are measure of the number of NSs at the surface which contribute to the multiple scattering[27,28]. The rapid increase in depolarization takes place when the average distances between NSs on the surface becomes small enough to enable multiple scattering of light. However, further reduction of the distance leads to the saturation of multiple scattering rate and in consequence to the saturation of $I^{av}_{VH}(t)$ and $I^{av}_{HV}(t)$. The applicability of the population function $I_B(t)$ in describing $I^{av}_{VH}(t)$ and $I^{av}_{HV}(t)$ intensities was confirmed with our experiments performed with different glycols and divers initial NSs concentrations (see Figure 5).

Evolution of scattered intensities with the polarization retained; the temporal Fano profile

The experimental $I_{VV}(t)$ and $I_{HH}(t)$ intensities display regular Whispering Gallery Mode oscillations (e.g.[13]) around the $I^{av}_{VV}(t)$ and $I^{av}_{HH}(t)$ averages (Figure 4 a). During the first stage of droplet
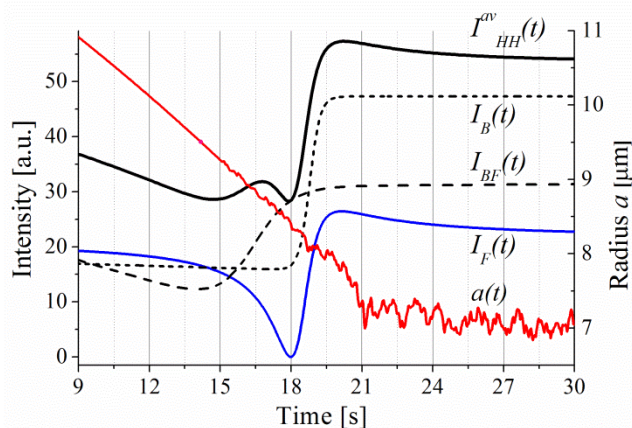
Figure 6 The averaged intensity $I^{av}_{HH}(t)$ and its decomposition into the Fano profile $I_F(t)$ (blue line) and the sigmoid profile $I_{BF}(t)$ (dashed line). The cross-polarized intensity $I^{av}_{HV}(t)=I_B(t)$ (short-dashed line) and the evolution of the droplet radius $a(t)$ (red) are shown for comparison.

evolution, up to ~13th second, (Figure 4 a)) $I^{av}_{VV}(t)$ and $I^{av}_{HH}(t)$ decrease linearly with time. At this stage, the intensity of scattered light is proportional to the droplet surface area ~a^2, while the droplet surface area diminishes linearly in time (see Figure 6) according to the "radius square law" (e.g.[29,30]). The next stage is characterised by $I^{av}_{VV}(t)$ and $I^{av}_{HH}(t)$ unusual dependence which includes fast increase at ~18th second and stabilisation which takes place visibly later than those of the cross-polarised intensities $I^{av}_{VH}(t)$ and $I^{av}_{HV}(t)$.

The average intensities $I^{av}_{VV}(t)$ and $I^{av}_{HH}(t)$ can be represented as a sum of $I_{BF}(t)+I_F(t)$ profiles. $I_{BF}(t)$ is the sigmoid-like, population function of time (compare Eq. (1)):

$$I_{BF}(t)=I_2(t)+\left(I_1(t)-I_2(t)\right)/(1+exp\left(\frac{t-t_0}{\Delta}\right)) \qquad (2)$$

with time-dependent $I_{1,2}(t)$ parameters. $I_1(t)$ is changing linearly with time (the "radius square law"), at the early evolution stage, while $I_2(t)$ describes changes of the scattered intensity at the final stage of drying NSs aggregate evolution. The increase visible in sigmoid-like function $I_{BF}(t)$ (Figure 6) corresponds to an increasing number of NSs populating the droplet surface. The populating slows down as a droplet surface area shrinks. $I_F(t)$ is the Fano profile:

$$I_F(t)=F\frac{(q\gamma+t-t_F)^2}{\gamma^2+(t-t_F)^2} \qquad (3)$$

where t_F and γ describe the central position and the width of the observed Fano profile respectively. The parameter q is, a so-called, Fano parameter, describing the degree of the profile asymmetry, F is a scaling factor. In Figure 6, an example decomposition of the average intensity $I^{av}_{HH}(t)$ into the sigmoid profile $I_{BF}(t)$ (grey line) and the Fano profile $I_F(t)$ (blue line) is shown. The fitted values of the Fano profile parameters are in this case q =0.49±0.06, t_F=18.4±0.1 s, γ=0.85±0.13 s, showing clearly the relevance of the Fano interference in the observed light intensity evolution. The sum of the sigmoid, population profile $I_{BF}(t)$ and the Fano profile $I_F(t)$ perfectly reproduces the temporal evolution of the $I^{av}_{VV}(t)$ and $I^{av}_{HH}(t)$ intensities (see Figures 5 and 6). The first, small maximum (at ~17th second in Figure 6)

results, in general, from a slight advance of the $I_{BF}(t)$ profile (with the centre at 16.3 s) in respect to the Fano $I_F(t)$ profile (with the centre at 19 s). This remains in agreement with the expected changes of the distribution of surface NSs, discussed in the previous Section (see Figure 3). NSs experience continuing rearrangement, due to the liquid evaporation. The changes of NSs distribution are reflected by the Fano interference (described by $I_F(t)$ profile) at the stage when NSs populate the droplet surface and become close enough to scatter light coherently. When the surface film composed of NSs is developing (Figure 3 c)), the change in the population profile $I_{BF}(t)$ translates to a small maximum of the observed $I^{av}_{VV}(t)$ and $I^{av}_{HH}(t)$ intensities (at ~17'th second in Figure 6, see also Figures 5 a), b), e), f)). However, in the case of small initial density of NSs (Figure 5 c), d)), the concentration of NSs is too small to form a regular film of NSs and the population function $I_{BF}(t)$ grows more slowly. In such case, the Fano profile defines the shapes of $I^{av}_{VV}(t)$ and $I^{av}_{HH}(t)$ intensities, which are then characterized by a single maximum.

It should be underlined that there is no indication of the Fano interference in $I^{av}_{VH}(t)$ or $I^{av}_{HV}(t)$ intensities of the depolarized scattered light. This means that the Fano profile is connected with the scattering process ($I^{av}_{VV}(t)$ and $I^{av}_{HH}(t)$), which does not depolarize light. Our experimental results show (see examples in Figure 5), that the Fano interference profile manifests for both H and V polarizations of laser light and for both light colours used in the experiment, regardless of the rate of solvent (glycols) evaporation and of the initial concentration of NSs. Moreover, the increase in $I_{BF}(t)$ population profiles, contributing to I^{av}_{HH} or I^{av}_{VV} intensities (with the centre at t_0~16.3 s), appear earlier then the increase seen in $I_B(t)$ profiles (with the centre at t_0~18.8 s) of the depolarised light intensities $I^{av}_{VH}(t)$ and $I^{av}_{HV}(t)$. It can concluded, that the increase in depolarization ($I_B(t)$ dependence) takes place for larger average distances between NSs on the surface than for $I_{BF}(t)$ and $I_F(t)$ profiles (scattered light with the polarization retained). This supports the interpretation that the observed depolarization is caused by multiple scattering which saturates for the densely packed NSs. The asymmetric scattering profile in I^{av}_{HH} or I^{av}_{VV} intensities appears as a result of single scattering on NSs being close enough to scatter light coherently at an average distances of the order of light wavelength.

Surface pressure and surface pressure isotherm

The thermodynamic-like modelling of the droplet of suspension can serve as an additional tool in the analysis of structural changes in NSs assemblies. The model describes the subsequent states of the droplet surface and is based on the analysis of the droplet radius evolution $a(t)$ found with use of Mie scattering theory. Optical diagnostics was supplemented at the late stages of evaporation by the data resulting from weighting the drying agglomerates (see Section 2). Knowing $a(t)$, we can find[12] the effective droplet surface pressure (activity) $p_{SP}=\sigma_L-\sigma$ defined as the difference of the effective surface tension σ of suspension and surface tension σ_L of pure liquid. In the case of evaporation of low-volatility liquids, the rate of change of the droplet surface area (proportional to $d(a^2(t))/dt$) can be approximated by[30]:

$$a(t)\frac{da(t)}{dt}=a\dot{a}(t)=-\Lambda D\frac{p_s}{T_a}exp(\frac{\Lambda}{T_a}\frac{2\sigma(t)}{a(t)}) \qquad (4)$$
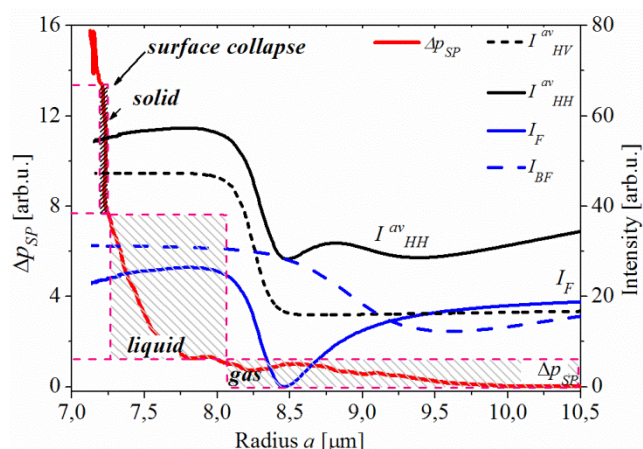
Figure 7 Changes in the surface pressure isotherm (left axis, red line) and the intensities $I^{av}_{HV}(a)$ and $I^{av}_{HH}(a)$ (right axis, grey and black lines) versus droplet radius a at the evolutions stage characterised by presence of the Fano $I_F(a)$ (blue solid) and the population $I_{BF}(a)$ contributions (blue dashed) to $I^{av}_{HH}(a)$.

where D is the diffusion constant, $\Lambda = M/(R\rho)$ and M and ρ are the molecular mass and density of liquid respectively, R is the universal gas constant and T_a is the temperature of droplet (surface), and p_s is the equilibrium vapour pressure. The evolution of the surface pressure p_{SP} resulting from eq. (3) is then[12]:

$$p_{SP}(t) = \sigma_L - \sigma(t) = \sigma_L + \frac{T_a}{2\Lambda} a(t) ln \left(\frac{a\dot{a}(0)}{a\dot{a}(t)} \right) \qquad (5)$$

where $a\dot{a}((0)) = -\Lambda D\, p_s/T_a$ is the evaporation rate of the droplet surface at $t=0$ which can be easily obtained from experimental data. So, the changes in $\Delta p_{SP}(t) = p_{SP}(t) - \sigma_L$ observed in the process of evaporation of the a droplet of suspension can be expressed with quantities derived from $a(t)$ evolution obtained from the experiment. It is worth noticing, that the effective surface pressure can serve as a measure of the mean distance between NSs. As the temperature T_a of a slowly evaporating droplet is constant[31], the $\Delta p_{SP}(a)$ dependence can be identified as the surface pressure isotherm.

An example of the surface pressure evolution $\Delta p_{SP}(a)$ as a function of droplet radius a is shown in Figure 7 (red) for the suspension of SiO_2 NSs in EG. We use the terms: surface gas, liquid and solid[12] to characterise the distribution of NSs on the droplet surface. Figure 7 illustrates the surface evolution stage when the mean distance between NSs becomes comparable to the wavelength of light. The following subsequent surface states can be identified by analysing the surface pressure isotherm (Figure 7, see also Figure 2 a)-d)):

a) the surface compressible gas of NSs (droplet size ~10.5μm down to ~8 μm), followed by surface gas–liquid phase transition - the change of the effective surface pressure is small,

b) the surface liquid of NSs (from a~7.8 μm to ~7.25 μm), combined with an increase of the surface pressure,

c) the surface solid of NSs - regular layer of NSs (a~7.25 μm), combined with a fast increase of the surface pressure (surface "crystallization"),

d) rearrangement of NSs in the droplet volume (volume

"crystallization") after a the collapse of the surface layer of NSs.

The surface states a)-d) correspond to the evolution stages observed in our numerical experiment illustrated in Figure 2 a)-d).

Finding the radius a, for which the collapse of the regular surface layer takes place (a=7200nm±150nm, see Figure 7) enables an estimate of the surface density of NSs at the evolution stage preceding the collapse. Under the assumption that the surface layer of NSs is close-packed (with packing factor 0.74), the estimated number of surface NSs is N_{sur}=760±30. This indicates that the average distances between surface NSs at the preceding stages (surface liquid and gas (Figure 7)) were of the order of the light wavelength.

The intensities $I^{av}_{HV}=I_B$ and I^{av}_{HH} of scattered light (Figure 4) together with the corresponding Fano profile I_F and population profile I_{BF} contributions to I^{av}_{HH} (Figure 4 and 6) are also shown in Figure 7, as the functions of the radius a. Their features show correspondence with the surface states identified from the surface pressure isotherm $\Delta p_{SP}(a)$. The rapid increase of the depolarized light intensity I^{av}_{HV} (and thus of $I_B = I^{av}_{HV}$, (Eq.(1)), appears during the surface state a) of compressible gas just before the formation of the surface liquid of NSs. Stabilisation of cross-polarised intensities coincides with the state b) of NSs surface liquid. As we have attributed the depolarization of light to multiple scattering, it indicates that the increase of multiple scattering corresponds to a dense but still compressible gas state of surface NSs when the mean distances between NSs are not minimal yet.

Furthermore, the transition from the state a) of the compressible surface gas of NSs (Figure 7) to the state b) of NSs' surface liquid coincides with the transition from negative to positive Fano interference and with the increasing density of surface NSs (seen in I_F profile). Closely spaced NSs contribute to the coherent single-scattering in line with our description given in previous sections.

Our analysis of the surface states dynamics in terms of changes of the surface pressure is qualitative in its character. It is intended to reinforce our interpretation of the observed optical effects and the appropriateness of our numerical modelling of the evaporation driven aggregation of nanoparticles. The reported phase behaviour of films of silica particle on the spherical air-glycol interface, driven by droplet evaporation, is analogous to widely studied phase transitions in the Langmuir and Langmuir-Blodgett quasi-two-dimensional flat films of nanospheres upon compression (e.g. [32, 33]). A surface pressure isotherm is one of the major experimental techniques used in this field to examine the phase transitions in such films. However, silica NSs are usually studied on the air-water interface (e.g. [34-37]change) rather than on air-glycol interfaces.

The method of studying changes of the surface pressure used in this paper offers a promising technique for studying colloidal films on spherical air-liquid interfaces on the new basis. However, in order to get quantitative results, further study is still needed.

Conclusions

Observation of the process of evaporation of a single, levitating microdroplets of glycols containing SiO_2 nanospheres, allowed us to study the interference processes which lead to the characteristic asymmetric temporal profiles of the intensities of the scattered laser light. This asymmetry of the intensity of linearly polarized scattered light (preserving the polarization of the incident light) was attributed to the Fano interference. For the first time we demonstrated the existence of the temporal Fano profile, resulting from the constructive and destructive interference between long and short lasting scattering processes occurring during the evaporation of a droplet of suspension. The effect was observed in time domain at a frequency of the elastically scattered laser light in contrast to the original profile identified by Ugo Fano[1-4] in the scattering spectrum. The asymmetry of the profile correlates with the growing population of nanospheres on the shrinking droplet surface and the formation of a dense surface layer of NSs. The absence of the Fano profile in the intensity of depolarized scattered light confirms that the observed dynamic effect is due to the interference processes. The Fano profile arises as a result of the interference which develops as the mean distance between NSs on the surface of an evaporating droplet diminishes to the range of the wavelength of light.

Our interpretation of the origin of the observed temporal Fano profiles is supported by the thermodynamic-like description in terms of the effective surface pressure isotherm applied to the droplet surface modified by emerging NSs. The analysis of successive surface states indicates that the Fano interference is connected with the formation of a compressible state of surface gas of NSs and its transition to the liquid-like state. Also, the performed numerical simulations of the changes in the distribution of NSs correlate with the derived surface pressure isotherm and with the results of the optical measurements. The changes in NPs distribution at the wavelength scale influence both the single-scattering and multiple-scattering processes. Single-scattering leads to the observed Fano interference superimposed on the population changes of NSs emerging on the droplet surface and forming a regular layer (distance between NSs comparable to the light wavelength). Multiple scattering causes depolarisation of light which follows the sigmoidal (step-like) function of the time of evaporation.

The reported study can serve as the basis for a wide range of methods of diagnostics of configuration changes in complex systems of nano- and microparticles with distances evolving at the light wavelength scale (e.g. [38]). In particular, we are convinced that the reported temporal Fano profile can be of the same importance to the scattering of waves by evolving complex systems as is the well-known asymmetric Fano profile observed in the spectra of scattered light.

Acknowledgements

Notes

*Institute of Physics, Polish Academy of Sciences, Al. Lotników 32/46, 02-668 Warszawa, Poland. Fax: (+48) 22 843 09 26; Tel: (+48) 22 116 33 19; E-mail: Krystyna.Kolwas@ifpan.edu.pl

References

1. U. Fano, Nuovo Cimento 1935, **12**,154 –161.
2. T. B. Dinh, K. D. Quoc, V. C. Long, K. D. Xuan, EPJ Special Topics 2013, **222**, 2233–2239.
3. E. Miroshnichenko, S. Flach, and Y. Kivshar, Rev. Mod. Phys. 2010, **82**, 2257–2298.
4. B. Luk'yanchuk, N. I. S. Zheludev,. A. Maier, N.J. Halas, P. Nordlander, H. Giessen, and Chong Tow Chong, Nature Materials 2010, **9**, 707–715.
5. K. F. Brennan, The Physics of Semiconductors with Applications to Opto-electronic Devices 1999 (Cambridge University Press).
6. V. M. Shalaev, Optical Properties of Nanostructured Random Media 2002 (Springer: Berlin).
7. E. Wolf, Progress in Optics 47, 2005, Elsevier.
8. V. M Shalaev, Nature photonics 2007, **1**, 41– 48.
9. S. M. Auerbach, K.A. Carrado, and P. K Dutta, Photonic crystals molding the flow of light 2008 (Princeton University Press, Princeton).
10. S. M.; Carrado, K.A. Auerbach, and P. K. Dutta, Handbook of Layered Materials 2004 (Taylor & Francis).
11. G. Derkachov, K. Kolwas, D. Jakubczyk, M. Zientara, and M. Kolwas, J. Phys. Chem. C 2008, **112**, 16919–16923.
12. D. Jakubczyk, M.Kolwas, G. Derkachov, and K. Kolwas J. Phys. Chem. C 2009, **113**,10598–10602.
13. M.Kolwas, D. Jakubczyk, G.Derkachov, and K. Kolwas, J.Q.S.R.T. 2013, **131**, 138 – 145.
14. W. Paul, Rev. Mod. Phys. 1990, **62**, 531–540.
15. D. J. Berkeland, J. D. Miller, J. C. Bergquist, W. M. Itano, and D. J. Wineland, J. Appl. Phys. 1998, **83**, 5025– 5033.
16. E. J. Davis, M. F. Buehlerand T. L. Ward, Rev.Sci. Instrum. 1990, **61**, 1281– 1288.
17. S. Arnold, Rev.Sci. Instrum.1991, 62, 3025-8.
18. D. Jakubczyk, G. Derkachov, T. Do Duc, K. Kolwas, and M. Kolwas J. Phys. Chem. A 2010, **114**, 3483–3488.
19. D. Jakubczyk, G. Derkachov, M. Kolwas, and K. Kolwas, J.Q.S.R.T. 2013, **12**, 99 – 104.
20. D. Jakubczyk, G. Derkachov, M. Zientara, M. Kolwas, and K. Kolwas J. Opt. Soc. Am. A 2004, **21**, 2320–2323.
21. H. Ulmke, T. Wriedt, and K. Bauckhage Chem. Eng. Technol. 2001, **24**, 265–268.
22. H. Ulmke, T. Wriedt, H. Lohner, and K. Bauckhage Proc.1st EUSPEN Conference 1999, **2**, 290–293.
23. G. Brenn, Chem. Eng. Sci. 2000, **55**, 5437–5444.
24. C. F. Bohren and D. R Huffman,. Absorption and Scattering of Light by Small Particles 2008 (Wiley).
25. M.I. Mischenko, Electromagnetic Scattering by Particles and Particle Groups 2014 (Cambridge University Press).
26. http://mathworld.wolfram.com/PopulationGrowth.html
27. C.M. Sorensen, Aerosol Science and Technology 2001, **35**, 648-687
28. M.I. Mischenko, J.Q.S.R.T. 2009, **110**, 1210-1222
29. D. Jakubczyk, G. Derkachov, M. Kolwas, K. Kolwas and M. Zientara, Acta Physica Polonica A 2012, **22**, 709-716.
30. Pruppacher; Klett, J. Microphysics of Clouds and Precipitation 1997 (Kluwer, Dordrecht).
31. G. Derkachov, D. Jakubczyk, M. Woźniak, J. Archer, M. Kolwas, J. Phys. Chem. B 2014, **118**, 12566−12574.
32. A. W. Adamson and A. P. Gast, Physical Chemistry of Surfaces. John Wiley & Sons, 1997
33. Ed. A. S. Hamdy Makhlouf and I. Tiginyanu, Nanocoatings and Ultra-Thin Films: Technologies and Applications, Elsevier, 2011
34. K. Wostyn, Y. Zhao, G. De Schaetzen, L. Hellemans, N. Matsuda, K. Clays, and A. Persoons, Langmuir, 2003, **19**, 4465–4468.
35. R. Miller, V. B. Fainerman, V. I. Kovalchuk, D. O. Grigoriev, M. E. Leser, and M. Michel, Adv. Colloid Interface Sci. 2006, **128–130**, 17–26.
36. M. Safouane, D. Langevin, and B. P. Binks, Langmuir, 2007, **23**, 11546–11553,
37. E. Guzmán, L. Liggieri, E. Santini, M. Ferrari, and F. Ravera, J. Phys. Chem. C, 2001, **115**, 21715–21722.

38 F.R.A. Onofri, S. Barbosa, O. Toure, M. Woźniak, C. Grisolia, J. Q.
    S. R. T. 2013, **126**, 160–168.